Article:

Deng 邓, R 仁, Mori, K., Miao, E. et al. (2026) Broadband x-ray observations of the periodic optical source ZTF J185139.81+171430.3 and its identification as a massive intermediate polar. The Astrophysical Journal, 997 (2). 166. ISSN: 0004-637X

https://doi.org/10.3847/1538-4357/ae2ac6

The Astrophysical Journal, 997:166 (10pp), 2026 February 1 https://doi.org/10.3847/1538-4357/ae2ac6

Broadband X-Ray Observations of the Periodic Optical Source ZTF J185139.81+171430.3 and Its Identification as a Massive Intermediate Polar

Ren Deng (邓仁)[1], Kaya Mori[1], Eric Miao[1], Gabriel Bridges[1], Charles J. Hailey[1], David A. H. Buckley[2,3,4], Gavin Ramsay[5], and Dan Jarvis[6]
[1] Columbia Astrophysics Laboratory, Columbia University, New York, NY 10027, USA
[2] South African Astronomical Observatory, P.O Box 9, Observatory, 7935 Cape Town, South Africa
[3] Department of Astronomy, University of Cape Town, Private Bag X3, Rondebosch 7701, South Africa
[4] Department of Physics, University of the Free State, PO Box 339, Bloemfontein 9300, South Africa
[5] Armagh Observatory and Planetarium, College Hill, Armagh, BT61 9DG, UK
[6] Astrophysics Research Cluster, School of Mathematical and Physical Sciences, University of Sheffield, Sheffield S3 7RH, UK

Received 2025 June 26; revised 2025 December 8; accepted 2025 December 8; published 2026 January 21

Abstract

We present X-ray observations of the periodic optical source ZTF J185139.81+171430.3 (hereafter ZTF J1851) by the XMM-Newton, NICER, and NuSTAR telescopes. The source was initially speculated to be a white dwarf (WD) pulsar system, due to its short period ($P \sim 12$ minutes) and highly modulated optical lightcurves. Our observations revealed a variable X-ray counterpart extending up to 40 keV with an X-ray luminosity of $L_X \sim 3 \times 10^{33}$ erg s^{-1} (0.3–40 keV). Utilizing timing data from XMM-Newton and NICER, we detected a periodic signal at $P_{\rm spin} = 12.2640(7) \pm 0.0583$ minutes with $>6\sigma$ significance. The pulsed profile displays ~25% and ~10% modulation in the 0.3–2 and 2–10 keV bands, respectively. Broadband X-ray spectra are best characterized by an absorbed optically thin thermal plasma model with $kT \approx 25$ keV and a Fe K-α fluorescent line at 6.4 keV. The bright and hard X-ray emission rules out the possibility of a WD pulsar or ultra-compact X-ray binary. The high plasma temperature and Fe emission lines suggest that ZTF J1851 is an intermediate polar spinning at 12.264 minutes. We employed an X-ray spectral model composed of the accretion column emission and X-ray reflection to fit the broadband X-ray spectra. Assuming spin equilibrium between the WD and the inner accretion disk, we derived a WD mass range of $M_{\rm WD} = (1.07–1.32)M_\odot$, exceeding the mean WD mass of IPs ($\langle M_{\rm WD}\rangle = 0.8M_\odot$). Our findings illustrate that follow-up broadband X-ray observations could provide unique diagnostics to elucidate the nature of periodic optical sources anticipated to be detected in the upcoming Rubin all-sky optical surveys.

Unified Astronomy Thesaurus concepts: DQ Herculis stars (407); Accretion (14); X-ray astronomy (1810); Cataclysmic variable stars (203); Compact objects (288)

1. Introduction

The Zwicky Transient Facility (ZTF) is one of the leading optical survey programs in contemporary time-domain astrophysics (E. C. Bellm et al. 2019). Since 2018, ZTF has provided wide-field coverage of the entire northern sky and discovered a number of supernovae, novae, and other transient objects. The vast ZTF lightcurve data in the *g*, *r*, and *i* bands also serve as a search engine for pulsating stars and binaries by detecting periodic signals. The high-cadence optical monitoring of more than a billion Galactic sources revealed a rare class of short-period objects with $P \lesssim 1$ hr. Some of these short-period objects turned out to be ultra-compact binaries (UCBs) with a white dwarf (WD) or neutron star (NS) primary, in addition to fast-spinning WDs. For example, the discovery of a 62 minute orbit black widow pulsar, where a millisecond pulsar ablates its companion via pulsar wind, highlights the potential of finding exotic binaries with ongoing optical surveys including the upcoming Rubin observatory Legacy Survey of Space and Time (K. B. Burdge et al. 2022).

Among the variable optical sources detected by ZTF, ZTF J1851 displayed a $P = 12.37$ minute periodicity with high modulation of ~0.8 mag (T. Kato & N. Kojiguchi 2021). In addition, several day-long outbursts with an increase in luminosity of ~2 mag have been detected (see Figure 1) by ZTF, GOTO, and ATLAS. In Figure 1, we also show L-band (400–700 nm) photometry obtained using the GOTO all-sky survey, which consists of 32 0.4 m telescopes located in La Palma in the Canaries and Siding Spring in Australia (D. Steeghs et al. 2022; M. J. Dyer et al. 2024). In addition, optical observations by ATLAS (J. L. Tonry et al. 2018) are displayed in Figure 1.

It is unknown whether the 12 minute periodicity represents a spin or orbital period, each of which would correspond to a different source type for ZTF J1851. In the spin period case, ZTF J1851 may be a cataclysmic variable (CV), an interacting binary harboring a WD accreting material from a Roche-lobe-filling late-type main-sequence companion. Magnetic CVs, either of the polar or intermediate polar (IP) types, emit copious X-rays with $L_X \gtrsim 10^{33}$ erg s^{-1} from their accretion columns in the form of thermal bremsstrahlung emission and atomic lines (K. Mukai 2017). Alternatively, the highly modulated, coherent periodicity in the optical band suggests that ZTF J1851 could be another WD pulsar spinning at $P = 12.37$ minutes. Unlike magnetic CVs, the only two known WD pulsar systems, AR Sco and J191213.72-441045.1,

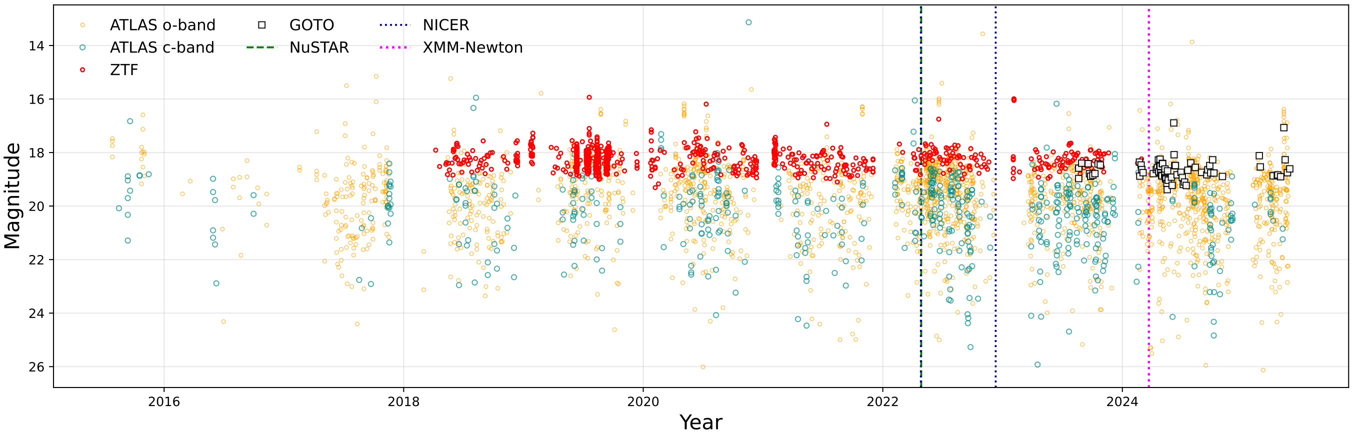

Figure 1. Long-term optical lightcurve of ZTF J1851. Occasional day-long flares have been observed. The X-ray observation dates are marked by vertical lines.

exhibit faint X-ray emission ($L_X \sim 10^{30}$ erg s^{-1}), most likely of thermal origin (A. Schwope et al. 2023). For AR Sco, pulsed nonthermal X-ray emission below 2 keV was reported (J. Takata et al. 2021), consistent with magnetic dipole emission, rather than accretion.

In the orbital period case, ZTF J1851 could be a UCB containing either a WD (AM CVn) or an NS (UCXB). AM CVn stars are close binary systems with $P_{\rm orb} \lesssim 1$ hr, composed of a WD and a low-mass companion. Apart from the direct impact systems, HM Cnc and V407 Vul, which show strong soft X-rays with $kT_{\rm BB} < 0.1$ keV, AM CVn binaries typically show thermal bremsstrahlung emission with $kT_{\rm max} \sim 5-6$ keV (G. Ramsay et al. 2005). On the other hand, NS-UCBs are accreting NS binaries with tight orbits ($P_{\rm orb} \lesssim 1$ hr). Among ~40 known UCXBs and candidates, including 15 sources confirmed through observed type I X-ray bursts, only three sources have $P_{\rm orb} \lesssim 30$ minutes (F. Koliopanos et al. 2021). ZTF J1851 resembles a 12.8 minute orbit UCXB candidate (OGLE-UCXB-01) discovered by the OGLE optical survey and also detected in the X-ray band by Chandra (P. Pietrukowicz et al. 2019), with similar X-ray luminosities, high optical modulation, and occasional optical flares. These known UCXBs show power-law X-ray spectra with either no or weak Fe K emission lines (EW < 100 eV) reflected off the accretion disk (F. Koliopanos et al. 2021).

Follow-up X-ray observations of ZTF J1851 are important for elucidating the source type. We performed X-ray observations and detected an X-ray counterpart with NuSTAR, NICER, and XMM-Newton in 2022–2024. In this paper, we present the first X-ray spectral and timing analysis of ZTF J1851 using broadband X-ray data. In Section 2, we describe the X-ray observations and data processing. In Section 3, we describe our X-ray timing analysis, searching for an X-ray periodicity and characterizing X-ray lightcurves. In Section 4, we describe various source type candidates for ZTF J1851 and identify it as an IP based on its X-ray timing and spectral properties. With phase-averaged and phase-resolved spectral analysis, we constrain several critical physical parameters, including metallicity, plasma temperature, and Fe emission lines. In Section 5, we discuss the implications of our timing and spectral analysis results. In Section 5.2, we employ our physically motivated spectral model for constraining the WD mass of ZTF J1851. Finally, we conclude the paper with future prospects in Section 6.

Table 1
X-Ray Observations of ZTF J1851

Observation Date	Telescope	ObsID	Exposure (ks)
2022-04-28	NuSTAR	30801008002	42.6
2022-04-27/28	NICER	559401010[a]	9.5
2022-12-11/13	NICER	559401020[a]	5.7
2024-03-22	XMM-Newton	0921690101	79

Note.
[a] NICER observations are collected in several successive observations sharing the same obsID prefix.

2. X-Ray Observations and Data Reduction

ZTF J1851 was observed by NuSTAR (42.6 ks) and NICER (9.5 ks) in 2022 April, and was subsequently observed by XMM-Newton in 2024 March (79 ks) (Table 1). Figure 1 shows the optical lightcurve of the source, overlaid with vertical lines indicating X-ray observation dates. For NuSTAR, we processed the data using `nupipeline` (F. A. Harrison et al. 2013). For timing and spectral analysis, we extracted source events from a $r = 12''$ circle around the source position. Background events were extracted from a source-free $r = 107''$ circle region on the same detector chip where the source is located. The NuSTAR data were contaminated by background above 35 keV. We collected ~1000 source counts after background subtraction. For XMM-Newton data, we reduced the datasets using SAS 21.0. We utilize *emchain* and *epchain* for GTI filtering for MOS and PN cameras, respectively. After filtering, this leaves an exposure time of about 54 ks for PN camera and 74 ks for MOS cameras. We extracted a source region with a circle of radius $r = 400''$, with an annular region of $r = 500''$–$1500''$ used for background extraction. We collected ~7100 and ~10,000 source counts in the combined MOS and PN cameras, respectively. We processed the NICER data using the `nicerl2` and `nicerl3-spect` tasks in the NICER Data Analysis Software (`NICERDAS`

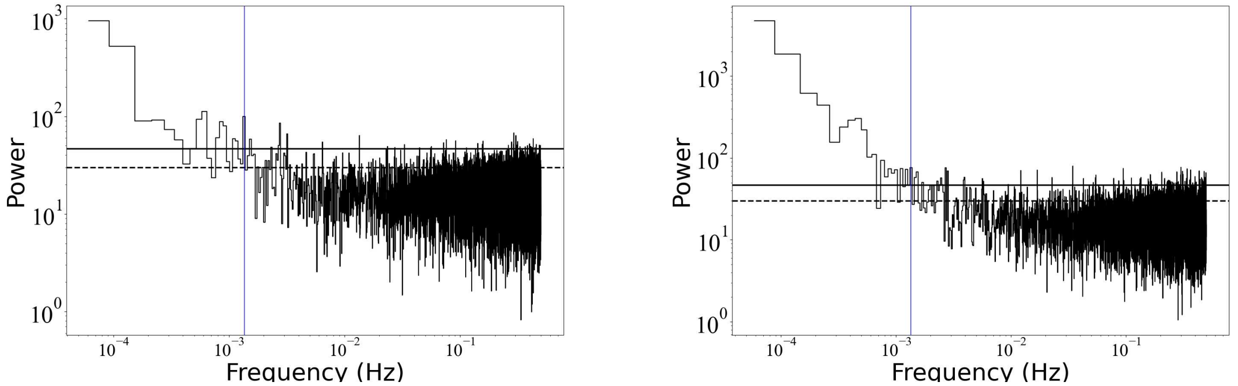

Figure 2. PDS periodograms obtained from the combined MOS (left) and PN (right) cameras. Blue vertical line marks the known optical periodicity $P = 12.37$ minutes. Note that both axes are in log scale. The dashed and solid lines denote the 3σ and 5σ significance, respectively.

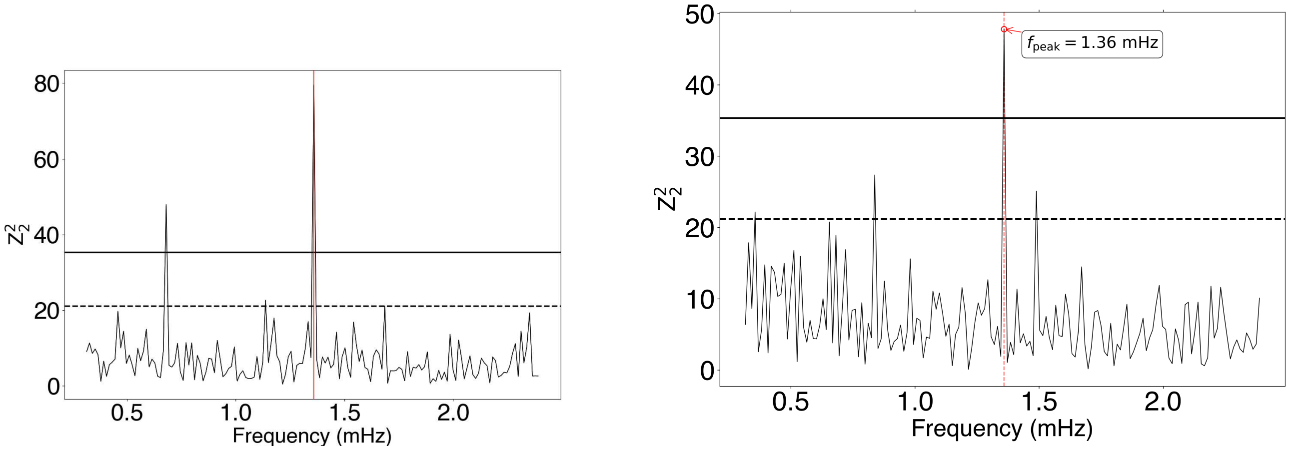

Figure 3. Z_2^2 soft X-ray (0.3–2 keV) periodograms. Left: combined MOS cameras. Right: PN camera. The red vertical line marks the most significant peak. The dashed and solid lines denote the 3σ and 5σ significance, respectively.

version 13). For NICER, the `SCORPEON` background model was used when fitting spectral data. We discarded the December NICER observations because their photon counts are close to zero. For April observations, we used only observations 5594010103 and 5594010104.

3. Timing Analysis

We performed timing analysis on the X-ray observation data using the `Stingray` (D. Huppenkothen et al. 2019; M. Bachetti et al. 2024) and `Hendrics` (M. Bachetti 2018) software packages. First, we applied barycentric corrections to all extracted source events using the SAS command barycen for the XMM-Newton data and the HEASOFT command barycorr for the NuSTAR and NICER data.

3.1. Periodicity Search

We conducted the Z-test for $n = 1$, 2, and 3 harmonic components using the weighted Z_n^2 function through **z_n_search** in `Stingray`. No significant periodicity was detected in the NuSTAR data (3–40 keV), likely due to the lower source counts. We adopted $n = 2$ for the number of harmonics in the Z^2 test for XMM-Newton. Including higher harmonic components did not improve the Z^2 statistics. The power density spectra (PDS) over a broad frequency band are dominated by red noise below $f \lesssim 10^{-3}$ Hz, yielding no significant peak detection (Figure 2). We conducted a refined period search in a narrower frequency range ($f = 0.5$–2.5 mHz) around the optical period at $P = 12.37$ minutes corresponding to $f \approx 1.36$ mHz (Figure 3). We detected a significant periodic signal ($>6\sigma$) at the $P = 12.26$ minute period below 2 keV in the PN data. The signal was detected with $>8\sigma$ significance in the combined MOS data. Above $E = 2$ keV, the periodic signal was detected in the XMM-Newton data with lower significance ($\sim 5\sigma$). In the narrowband Z^2 data, we fit the 12.26 minute peak with a Gaussian and constrain its width to $\Delta f < 0.014$ mHz. As the frequency resolution is defined by the reciprocal of the observation time, the measured period $P_{\mathrm{spin}} = 12.2640(7) \pm 0.0583$ minutes is well-constrained due to the long baseline of 70 ks XMM-Newton observation time.

Notably, this measured X-ray period ($P = 12.26$ minutes) very significantly differs from the previously known optical period at $P = 12.37$ minutes. In addition, both the XMM-Newton and NICER data showed no noticeable modulation when folded at the optical period of $P = 12.37$ minutes. After investigating possible aliases, we identified the optical period as simply the one-day alias of the X-ray period. This is expected for single-site (ZTF) data. Thus, we conclude that the X-ray period of $P = 12.26$ minutes represents the intrinsic periodicity of ZTF J1851.

For the NICER data, we used the `Hendrics` command HENzsearch to attempt to conduct Z^2 tests, with $n = 1$ for the number of harmonics. Inspecting the entire observational lightcurve revealed short GTIs of $\sim$15 minutes in length,

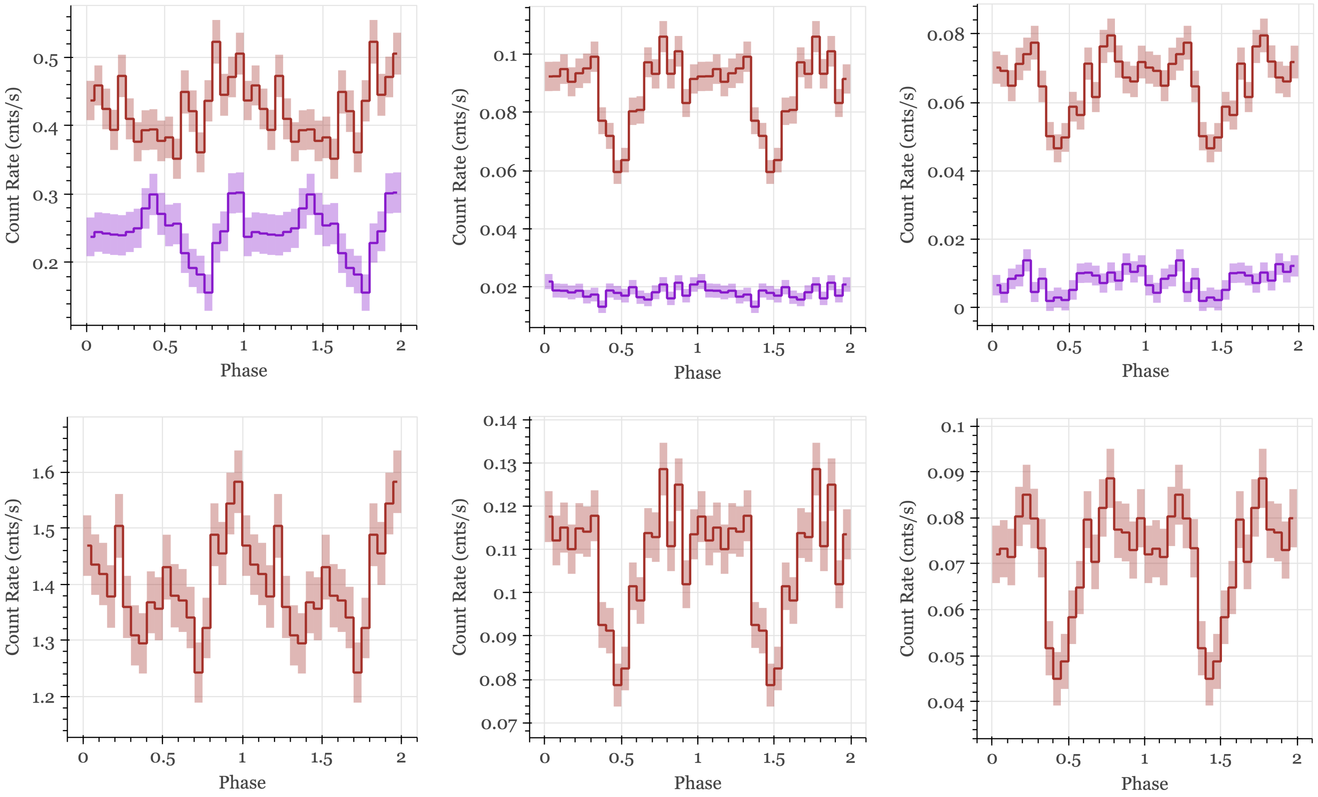

Figure 4. Folded lightcurve plots in the soft (0.3–4 keV for XMM-Newton and 1–4 keV for NICER; red) and hard (4–10 keV; purple) X-ray bands, with 1σ error bars shown (left: NICER; middle: XMM-MOS; right: XMM-PN). The bottom three figures show the combined folded lightcurves including photon energy up to 10 keV. All lightcurves are folded over the P = 12.26 minute period, have been phase-aligned, and contain 20 bins per phase.

spaced ∼93 minutes apart. As a result, we also utilized `astropy's` LombScargle to conduct a floating-point Lomb–Scargle test (N. R. Lomb 1976; J. D. Scargle 1982) at 20 s per bin. Both pulsation searches gave similar results, with statistically insignificant ($<1\sigma$) peaks detected at the measured X-ray frequency ($f \approx 1.36$ mHz). A possible explanation is the dominance of the ISS period and its harmonics ($f \sim n^{*}0.18$ mHz) on both spectra, obscuring the significance of the signal frequency.

3.2. Folded X-Ray Lightcurves

Using `Stingray`'s **fold_events**, we produced exposure-corrected pulsed profiles folded at P = 12.26 minutes for NICER, PN, and MOS data separately. For XMM-Newton, we subtracted the source profile with a background profile normalized using the BACKSCAL and AREASCAL values from the spectral files. For NICER lightcurves, we folded the estimated background lightcurve produced by the SCORPEON background model in nicerl3-lc, and subtracted it from the total profile. Subtracting out backgrounds ensures accurate determination of pulsed fractions and hardness ratios.

Folded lightcurves in the 0.3–4 keV and 4–10 keV energy bands are shown in Figure 4, each with 20 bins per phase. For NICER, we used 1–4 keV for the soft energy band, since photon counts below 1 keV are dominated by background. The pulse fraction is defined as $\frac{a-b}{a+b}$, where a and b are respectively the minimum and maximum of the profile. Soft and hard X-ray lightcurves from XMM-Newton exhibit a pulse fraction between 20% and 25%, and NICER lightcurves exhibit a comparable pulse fraction of ∼20% in the soft band but a stronger 30% in the hard band. Significant periodic modulation in the NICER folded lightcurves demonstrates the existence of a 12.26 minute period despite insignificant Z^2 and Lomb–Scargle tests.

Using count rates from the folded profiles, we calculated hardness ratios folded at the P = 12.26 minute period. The hardness ratio is defined as $\frac{\text{hard} - \text{soft}}{\text{hard} + \text{soft}}$, where "soft" and "hard" are the soft and hard energy band count rates for the respective telescope. In the XMM-MOS plot (Figure 5, left panel), we observe that the hardness ratio anticorrelates with the overall lightcurve data—for example, the hardness ratio is peak at $\phi \approx 0.5$ where the X-ray flux dips.

4. Spectral Analysis

We present phase-averaged and phase-resolved X-ray spectral analysis using XMM-Newton, NuSTAR, and NICER data. We jointly fit the NuSTAR, XMM-Newton, and NICER data in 0.3–30 keV spectra with phenomenological models to constrain the spectral properties. For NICER spectra, we ignored low-energy photons below 1 keV, as the measured flux is lower than the flux predicted by the `SCORPEON` background model. The NICER observations from 2022 December were discarded due to their short GTIs (minutes) and lack of source counts. The results of fitting our phenomenological models are summarized in Table 2. We performed spectral fitting with `XSPEC` version 12.13.1 (K. A. Arnaud 1996). Each spectral model was multiplied by `tbabs` to account for the ISM absorption using the Wilms abundance data (J. Wilms et al. 2000). In addition, `constant` was applied as a cross-

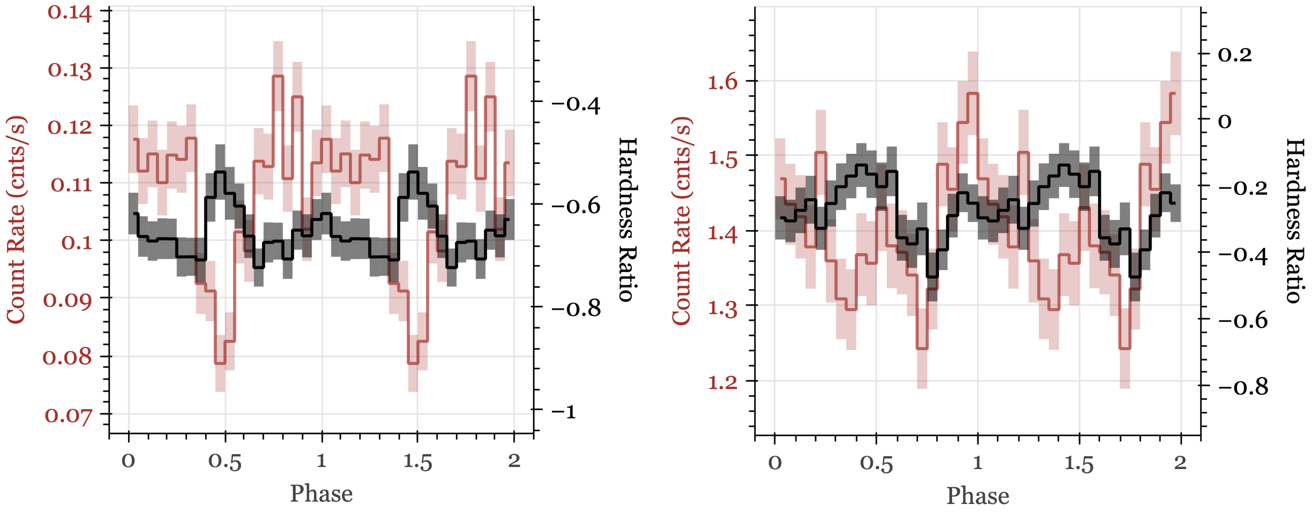

Figure 5. The hardness ratios (black) overlaid with the 0.3–10 keV (left: XMM-MOS) and 1–10 keV (right: NICER) folded lightcurves, showing an anticorrelation. Both are folded at the $P = 12.26$ minute period. The hardness ratio is defined as $\frac{\text{hard} - \text{soft}}{\text{hard} + \text{soft}}$, where the soft and hard energy bands are defined as $E < 4$ keV and $E > 4$ keV.

Table 2
Phenomenological Model Fits to X-Ray Spectra

Parameter	`pow`	`APEC`	2·`APEC`	`APEC+bbody`	`APEC+Gauss`	`APEC+bbody+Gauss`
C_{XMM}[a]	0.64	0.63	0.62	0.64	0.63	0.62
C_{NuSTAR}[a]	0.96	1.03	0.94	0.92	1.03	0.95
$N_{\text{H}}^{(i)}[10^{20}\ \text{cm}^{-2}]$[b]	8.99 ± 1.0	6.51 ± 0.7	6.77 ± 0.9	$8.82^{+0.9}_{-1.0}$	$6.66^{+0.7}_{-0.8}$	$8.62^{+1.2}_{-1.8}$
Γ	1.40 ± 0.04	…	…	…	…	…
kT_1 (keV)	…	$25.6^{+7.1}_{-4.8}$	$0.96^{+0.10}_{-0.08}$	$5.44^{+2.07}_{-1.06}$	$22.8^{+6.98}_{-3.45}$	$6.16^{+10.2}_{-1.72}$
kT_2 (keV)	…	…	$42.17^{+21.83}_{-10.72}$	$3.47^{+0.58}_{-0.39}$	…	$3.73^{+3.23}_{-0.61}$
$Z(Z_{\odot})$[c]	…	$1.02^{+0.59}_{-0.47}$	$1.78^{+1.76}_{-0.93}$	$0.16^{+0.16}_{-0.10}$	$0.90^{+0.57}_{-0.41}$	$0.18^{+0.57}_{-0.14}$
EW_{line}[d] (eV)	…	…	…	…	$208.7^{+68.5}_{-71.3}$	$153.0^{+58.3}_{-65.8}$
$F_X[10^{-13}\ \text{erg s}^{-1}\ \text{cm}^{-2}]$[e]	8.4	8.6	9.1	9.2	8.8	9.4
χ^2_ν (dof)	1.10 (763)	1.10 (762)	1.00 (760)	1.07 (760)	1.07 (761)	1.05 (757)

Notes. All errors shown are 90% confidence intervals.

[a] Cross-normalization factor of the XMM-Newton and NuSTAR data with respect to the NICER data.

[b] The ISM hydrogen column density associated with `tbabs`, which is applied to all models.

[c] Abundance relative to solar.

[d] The equivalent width of the Gaussian component with $E = 6.4$ keV and $\sigma = 0.01$ keV.

[e] The unabsorbed 3–10 keV flux of the NICER data.

normalization factor between the different X-ray observations, with respect to the NICER data.

4.1. Phase-averaged Spectral Analysis

First, we fit an absorbed power-law model Γ and yielded a fit with $\Gamma = 1.4$ and a reduced $\chi^2 = 1.10$ (Figure 6). Large residuals are present near 6–7 keV in NuSTAR and XMM-Newton spectra, indicating the presence of atomic lines. To confirm the presence of an atomic line in this regime, we compared the χ^2 of the best-fit models with and without a Gaussian component. Because an analytical F-test is not valid for assessing the significance of a line (R. Protassov et al. 2002; K. Mori et al. 2005), we used the Monte Carlo–based `simftest` command. We simulated 10^4 spectra drawn under the null hypothesis (assuming that no line is present); only two of the simulated spectra yielded a $\Delta\chi^2$ as large as observed when including a Gaussian model, exhibiting no significant improvement in fit statistic. Thus, the probability of obtaining an improvement in fit as large as observed by chance is $p < 2 \times 10^{-4}$ ($\approx 3.5\sigma$), strongly supporting the presence of a line unaccounted for by a power-law model alone. We then applied an absorbed optically thin thermal bremsstrahlung model with atomic lines (`APEC`). The improved spectral fit indicates a plasma temperature $kT \approx 25.6$ keV. A two-temperature model (`APEC+APEC`) did not improve the fit with $kT_1 \sim 1$ keV and $kT_2 \sim 40$ keV. We also added a Gaussian line at 6.4 keV or a blackbody component (`bbodyrad`), as they are occasionally observed from X-ray spectra of mCVs. The 6.4 keV Gaussian line accounts for the neutral Fe K-α line from X-rays reflected off the WD surface or accretion curtain. This atomic line is most visible in NuSTAR and XMM-Newton spectra (Figure 6). The fit was marginally improved ($\chi^2_\nu = 1.07$) with the equivalent Gaussian width ($\text{EW} = 208.7^{+68.5}_{-71.3}$ eV). The blackbody radiation could arise from the heated polar caps on the WD surface (S. Scaringi et al. 2010). However, the best-fit blackbody temperature ($kT_{\text{BB}} = 3.5$ keV) far exceeded the typical blackbody temperatures for mCVs ($kT_{\text{BB}} \lesssim 0.1$ keV; G. Ramsay & M. Cropper

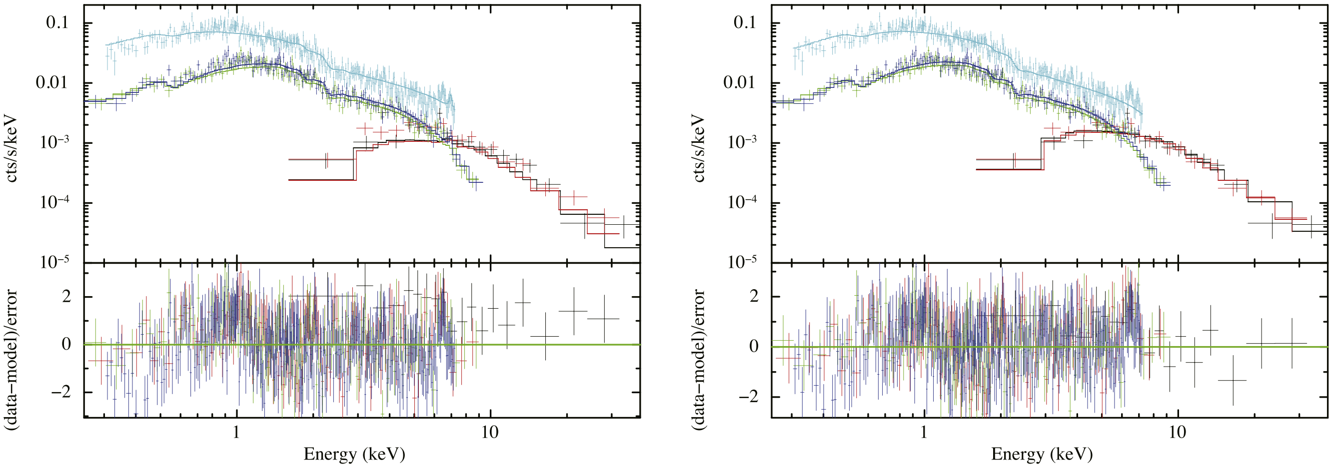

Figure 6. Joint XMM-Newton (light blue: pn; green: MOS1; dark blue: MOS2) and NuSTAR (black: FPMA; red: FPMB) spectra fitted by absorbed `APEC` (left) and absorbed power-law (right) models. Notice the atomic line between 6 and 7 keV in the residual. NICER spectra are excluded in the figures to highlight the atomic lines, but they are included in the phenomenological fittings.

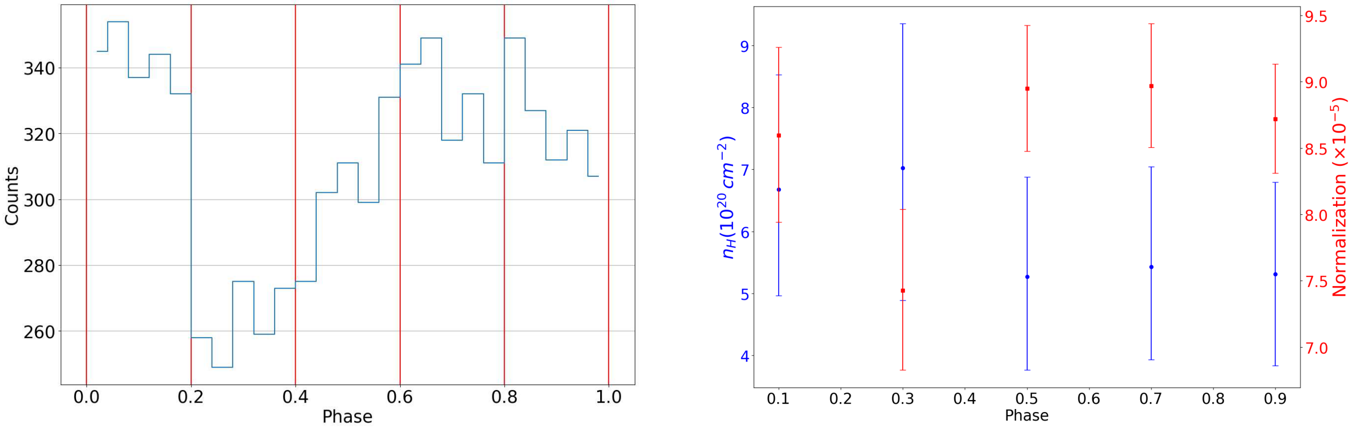

Figure 7. Results of phase-resolved spectroscopy. Left: The PN camera lightcurve folded at the 12.27 minute period, with red lines demarcating the five phase bins ($\phi = 0.0$–0.2, 0.2–0.4, 0.4–0.6, 0.6–0.8, and 0.8–1.0). Right: The variation of the best-fit hydrogen column density $n_{\rm H}$ and flux normalization across phase bins, with fixed $kT = 25.5$ keV and $Z = 1.0\ Z_\odot$.

2002). In NICER spectra, we found an emission line feature near 0.5 keV that does not have a counterpart in XMM-Newton observations. The emission line feature at 0.59 keV is likely caused by solar wind charge exchange (SWCX). Following guidance from the NICER helpdesk, we initially added an extra Gaussian line fixed at 0.59 keV to account for the neutral oxygen line when fitting NICER, XMM-Newton, and NuSTAR spectra jointly. We later discarded photons below 1 keV altogether, consistent with our timing analysis, as the `SCORPEON` model predicts background flux higher than the measured flux in that regime.

4.2. Phase-resolved Spectral Analysis

Given the ample photon statistics, we performed phase-resolved spectral analysis on the XMM-Newton data using the X-ray spin period ($P = 12.26$ minutes) detected in the XMM-Newton spectra. We extracted XMM-Newton spectra from five phase bins with $\Delta\phi = 0.2$ intervals and fitted an absorbed `APEC` model to each phase-resolved spectrum. We fixed the plasma temperature at the phase-averaged best-fit value $kT = 25.5$ keV and allowed the ISM hydrogen column density $n_{\rm H}$ to vary. The fits for all phase bins except the middle bin were excellent with $0.9 < \chi^2 < 1.1$, while the middle phase bin was subject to poorer fitting ($\chi^2 > 1.2$). We found a small anticorrelation between the X-ray absorption factor quantified by $n_{\rm H}$ and photon counts (Figure 7), with the highest X-ray absorption corresponding to the bin with the lowest photon counts. Likewise, the flux normalization factor exhibits an anticorrelation with $n_{\rm H}$ at fixed kT.

5. Discussion

We have thoroughly investigated the X-ray properties of the optical source ZTF J1851, using NuSTAR, XMM-Newton, and NICER data. Below, we discuss the results and implications of our preceding analysis.

5.1. Source Identification

The broadband X-ray spectra of ZTF J1851 display prominent atomic line near 6–7 keV and hard X-ray photons extending to ∼30 keV. The hard X-ray continuum observed by NuSTAR rules out the possibility of being a direct accretor like HM Cnc and V407 Vul or the disk-accreting AM CVns, which have more modest X-ray temperatures (G. Ramsay et al. 2005). The presence of prominent atomic lines is inconsistent with featureless power-law X-ray spectra observed in UCXBs (F. Koliopanos et al. 2021). The X-ray spectra of ZTF J1851 are also distinct from much fainter ($L_X \sim 10^{30}$ erg s^{-1}) and softer ($kT \lesssim 8$ keV) X-ray emission observed from the known WD pulsars (A. Schwope et al. 2023).

The bright X-ray luminosity ($L_X = 10^{33}$ erg s^{-1}), hard X-ray spectra, neutral and ionized Fe lines are all typically observed in IPs where the shock-heated accretion curtain emits thermal continuum X-rays and atomic lines. The high plasma temperature of $kT \approx 25$ keV is commonly observed from IPs, whose X-ray spectra are harder than polars or nonmagnetic CVs (C. J. Hailey et al. 2016; K. Mukai 2017). The neutral Fe fluorescent line, whose equivalent width (EW ∼ 200 eV) is typical among IPs, originates from X-rays reflected off the WD surface or accretion curtain. Knowing ZTF J1851 is an IP, it is also unlikely that the discrepancy between the measured X-ray and optical periods arises from the spin evolution of the WD between the optical period measurement in 2021 and the XMM-Newton observation in 2024. The indicated spin derivative of $\dot{P} \sim 10^{-9} s/s$, is several orders of magnitude higher than typically observed in mCVs (C. Salcedo et al. 2024), further validating that the optical period is the one-day alias produced by the Earth rotation. Furthermore, the energy-dependent X-ray modulation supports that the 12.26 minute period represents the WD spin. The higher pulsed fractions below 2 keV imply the presence of an accretion curtain that absorbs soft X-rays predominantly. In IPs, as accreting particles are funneled onto WD poles along magnetic field lines from the accretion disk or stream, they form an extended arc-like curtain of infalling gas that leads into the column. As the WD spins, the corotating accretion curtain absorbs soft X-rays and obscures the accretion column, causing the energy-dependent spin modulation and phase-dependent spectral hardening (S. R. Rosen et al. 1988). This is consistent with what we find in the energy-resolved lightcurve and hardness ratio plots (see Figures 4 and 5), where lower-energy lightcurves exhibit stronger modulation with the spin period, a feature commonly seen in IP systems (A. Joshi et al. 2022; C. Salcedo et al. 2024).

5.2. White Dwarf Mass Determination

Given that ZTF J1851 is an IP, we proceed to determine its WD mass in this section. In mCVs, X-ray emission is typically powered by mass accretion, with the infalling particles converting their gravitational potential energy into electromagnetic radiation via shock-heated gas flow. As the magnetic field disrupts the formation of a complete accretion disk, an accretion flow will be channeled along the magnetic field lines from the innermost accretion disk radius.

As the infalling gas reaches supersonic speed, a stand-off shock is formed and heats the gas. Subsequently, the shock-heated gas cools via cyclotron cooling and thermal bremsstrahlung radiation within the accretion column, which emits copious X-rays. Below the stand-off shock, a range of plasma temperatures, densities, and emissivity characterizes X-ray emission from the accretion column. This may be reflective of the fact that the two-temperature `APEC` model best fits the X-ray spectra, as shown in Table 2.

Following our recent IP papers (B. Vermette et al. 2023; C. Salcedo et al. 2024), we applied our latest 1D accretion spectral model `MCVSPEC` (G. Bridges et al. 2025, in preparation) for modeling X-ray emission from ZTF J1851. Its application for a polar is presented in L. W. Filor et al. (2025). Our model accounts for the gradient of plasma temperature, density, and X-ray emissivity within the accretion column self-consistently, as well as the effects of X-ray reflection off of the WD surface. The input parameters for `MCVSPEC` are M, f (fractional accretion area), L (bolometric luminosity [erg s^{-1}]), $P_{\rm spin}$ (WD spin period [s]), $Z/Z_{\odot}$ (abundance relative to solar), $\cos(i)$ (inclination angle of the reflecting surface), and flux normalization. Our model assumes that the gas particles acquire kinetic energy by falling from a finite magnetospheric radius (R_m) to the shock height (h). Therefore, the freefall velocity at the shock height is given by $v_{\rm ff} = \sqrt{2GM(\frac{1}{R+h} - \frac{1}{R_m})}$. This allows us to determine shock temperature ($T_{\rm s}$) and WD mass through the relation $kT_{\rm s} = \frac{3}{8}\mu m_H v_{\rm ff}^2$ (K. Aizu 1973; T. Hayashi & M. Ishida 2014; C. J. Hailey et al. 2016; V. Suleimanov et al. 2016; A. W. Shaw et al. 2020). In addition, some X-rays from the accretion column may be reflected by the WD surface or accretion curtain. These reprocessed X-rays manifest as a neutral Fe fluorescence line at 6.4 keV and a Compton scattering hump above ∼10 keV. The extent of X-ray reflection depends on the shock height: A tall accretion column diminishes the effects of reflection, since the viewing angle of the WD at a higher vantage point would be smaller. We account for this effect by internally implementing the X-ray reflection model (`reflect`) through the reflection fraction factor ($\Omega/2\pi$), where Ω is the solid angle of the WD surface viewed from the shock height (P. Magdziarz & A. A. Zdziarski 1995). Our overall spectral model is `tbabs*(MCVSPEC+Gauss)`, where the `reflect` model is implemented in `MCVSPEC`.

We estimate the magnetospheric radius using the results of our X-ray timing analysis. As we did not detect a spectral break associated with R_m in the PDS (V. Suleimanov et al. 2016), we assume that the innermost accretion disk corotates with the WD magnetosphere at R_m. Note that most IPs were found to be in spin equilibrium (J. Patterson et al. 2020). Hence, in the spin equilibrium assumption, we derive $R_m = R_{\rm co} = \left(\frac{GMP_{\rm spin}^2}{4\pi^2}\right)^{1/3}$. Since our initial work presented in B. Vermette et al. (2023), we have improved our model by internally calculating R_m from spin period to automatically fulfill our spin equilibrium assumption. For each iteration, then, our model uses the estimated mass M, R_m, and f to compute plasma temperature and density profiles within the accretion column by solving coupled differential equations associated with the mass, momentum, and energy conservation. The model keeps varying these parameters (M, R_m, and f) until the shock height is converged.

The systematic error associated with our mass measurement model arises from the unknown shock height, which is dependent on the uncertain specific mass accretion rate $\dot{m} = \frac{\dot{M}}{4\pi R^2 f}$, where $\dot{M}$ is the total mass accretion rate. At higher specific accretion rates $\dot{m}$, the gas density at the shock height increases, which lowers the speed of sound. As a result, the infalling gas takes longer to decelerate to the shock speed, causing the shock to form closer to the surface—that is, at a lower shock height. We derive the total accretion rate from the bolometric luminosity and WD mass through $L = GM\dot{M}(\frac{1}{R} - \frac{1}{R_m})$. The bolometric luminosity consists of bremsstralung emission L_X in the X-ray band and cyclotron emission $L_{\rm cyc}$ in the optical, IR, and UV bands. To

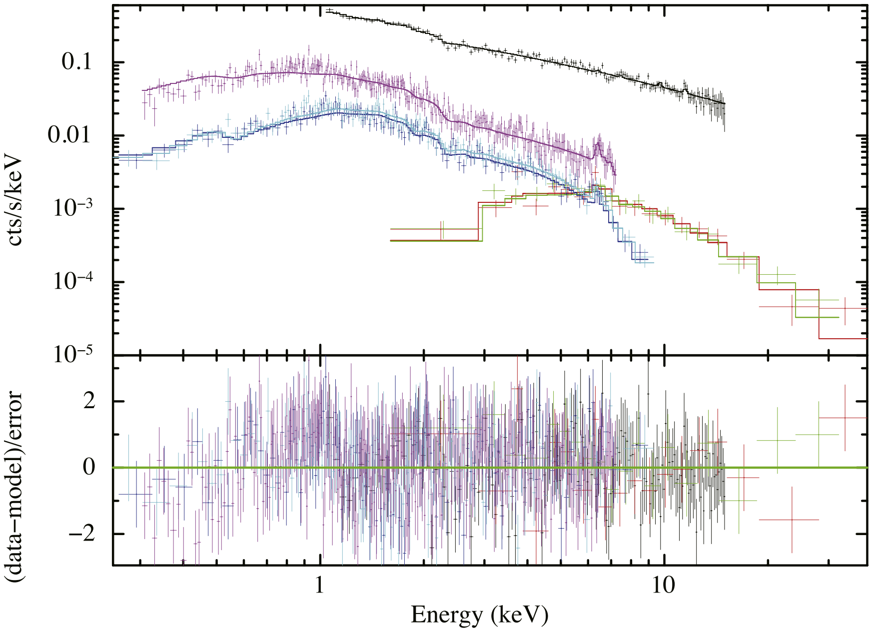

Figure 8. NICER (black), XMM-Newton (purple and blue), and NuSTAR (green and red) spectra of ZTF J1851 fit by the `tbabs*(MCVSPEC+Gauss)` model with a Gaussian component fixed at 6.4 keV ($\chi^2_\nu = 1.00$). For this particular case, corresponding to the fractional accretion area being fixed at $f = 4 \times 10^{-4}$, the best-fit WD mass is $M = 1.25 \pm 0.01\, M_\odot$, with $\dot{m} = 29.1$ g cm^{-2}s^{-1}. While the statistical error is quoted for the WD mass measurement above, the systematic error is considered in our final results by considering a range of the fractional accretion area.

obtain the X-ray luminosity, we employed the `cflux` model to find the unabsorbed X-ray flux, which for the NuSTAR data is $F_X = (2.6^{+0.4}_{-0.3}) \times 10^{-12}$ erg s^{-1} cm^{-2}. We used a `constant` factor to calculate the flux for the XMM-Newton datasets. Owing to the lack of UV- and IR-band observations, we estimate $L_{\rm cyc}$ with solely the optical luminosity, using ATLAS *o*-band and *c*-band fluxes that sum to $L_{\rm cyc} \approx 2.0 \times 10^{-13}$ erg s^{-1} cm^{-2} (Figure 1). Using the source distance of $d = 5$ kpc (C. A. L. Bailer-Jones et al. 2021), we determined $L = 8.4 \times 10^{33}$ erg s^{-1} and $\dot{M}$.

The unknown fractional accretion column area *f*, however, requires us to consider a range of *f* values that result in the systematic error associated with the WD mass measurement (C. Salcedo et al. 2024). The maximum possible fractional accretion area is $f_{\rm max} = \frac{R}{2R_m}$, assuming a dipole B-field geometry where the accreting gas falls from the entire accretion disk (J. Frank et al. 2002). For $M = 0.6 M_\odot$ and $P_{\rm spin} = 12.26$ minutes, we derived $f_{\rm max} \approx 0.04$,. Higher WD masses would yield $f_{\rm max} \sim 0.01 - 0.02$. The lower limit of *f* value, however, is less constrained. In mCVs, soft X-ray blackbody emission often arises from the accretion column base, which is heated by infalling gas particles (S. Scaringi et al. 2010), and its flux normalization can be used to estimate a *f* value. However, since we did not detect a blackbody emission component, we set a lower bound of the *f* value to 10^{-4} based on the theoretical estimates proposed by S. R. Rosen et al. (1988).

5.3. X-Ray Spectral Fitting Procedure

The input parameters for `MCVSPEC` for our optical source ZTF J1851 are generally unknown, with no previously determined magnetic field or inclination angle. Based on our phenomenological model fit results, we fixed the hydrogen column density $n_{\rm H}$ to 7×10^{20} cm^{-2} for the `tbabs` model. Following previous X-ray studies (e.g., C. J. Hailey et al. 2016), the Gaussian component used to model the neutral Fe fluorescence line is centered at 6.4 keV with fixed $\sigma = 0.01$ keV.

We test a wide range of $\dot{m}$ based on the bolometric luminosity and fractional accretion area. Since the mass accretion rate also depends on the initial mass estimate *M*, we must assume an initial WD mass (M_i) for fitting. To ensure our spectral fitting is self-consistent, we compare M_i with the `MCVSPEC` final mass fit (M_f) within their statistical and systematic error range. We sample four different initial masses with grid size $\Delta M_i = 0.2 M_\odot$, ranging from $M_i = 0.6 - 1.2 M_\odot$. We then iterate through different values of M_i and perform spectral fittings for each case, and we determine that lower initial masses at $M < 1.2 M_\odot$ fail to deliver self-consistent fittings. Representative best-fit spectra for a fixed fractional accretion area are presented in Figure 8. In Figure 9, which shows the best WD masses for various specific accretion rates for a given initial WD mass value ($M_i = 1.2 M_\odot$ in this case), all fittings have been performed with an initial guess $M_i = 1.2 M_\odot$, with a 90% error bar associated with each fit plotted. The blue shaded region is the total systematic and statistical error range, considering an unknown *f* value. We note that the region intersected by the red line represents the region where the systematic and statistical error of M_f subsumes M_i and is therefore self-consistent. Considering both the statistical and systematic error, this yields an estimated WD mass range of $M_{\rm WD} = (1.07\text{–}1.32) M_\odot$. Using the magnetic radius formula from (A. J. Norton et al. 2004), we further determine $B \sim 20\text{–}40$ MG. For descriptions of `MCVSPEC` fitting procedure applied to other mCVs, see L. W. Filor et al. (2025) or C. Salcedo et al. (2024).

The results of our spectral analysis using `tbabs*(MCVSPEC+Gauss)` are summarized in Table 3 and Figure 9 below. Notably, the best-fit WD mass saturates above $M = 1.1 M_\odot$ for sufficiently large specific accretion rate $\dot{m}$ (Figure 9). This saturation phase reflects the fact that, as $\dot{m}$ becomes large, the shock height becomes negligible.

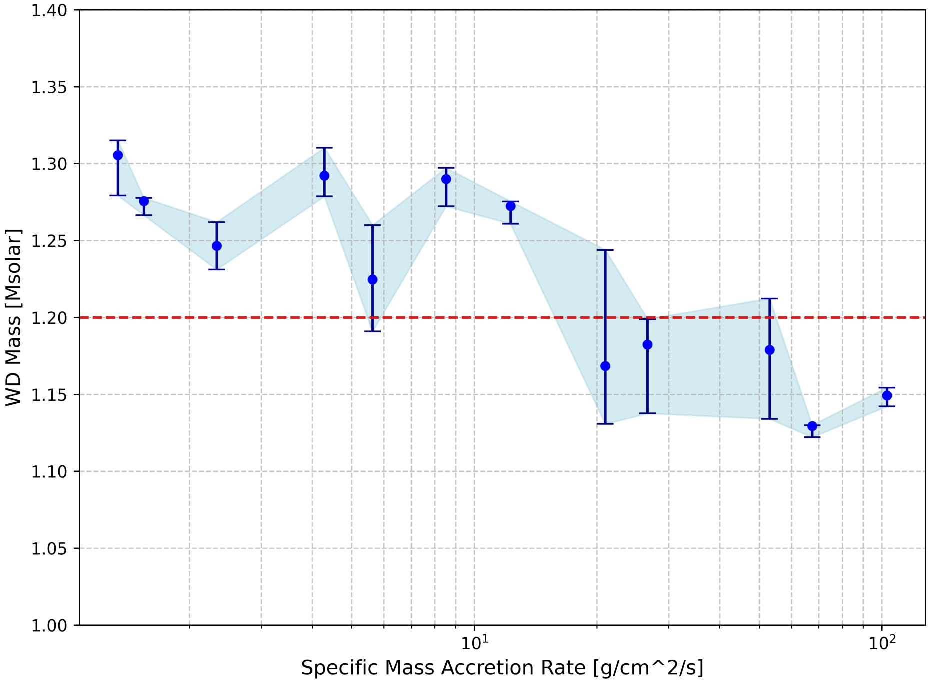

Figure 9. The best-fit WD mass as a function of $\dot{m}$ using `MCVSPEC` with a range of selected f values between $10^{-4} \leqslant f \leqslant 0.01$. In this case, we assumed an initial WD mass of $M_i = 1.2 M_\odot$ (red dashed line) and conducted spectral fitting. All cases yielded a reasonable fit to the X-ray spectra with $\chi^2_\nu = 1.0 - 1.1$, as shown in Figure 8.

Table 3
Selected `MCVSPEC` Fit Results to the X-Ray Spectra

Parameter	Case 1	Case 2	Case 3
$N_{\rm H}^{(i)}(10^{20}{\rm cm}^{-2})$[a,b]	7.0	7.0	7.0
f [b]	10^{-3}	2×10^{-3}	0.01
$\dot{m}_{\rm NICER}$ (g cm^{-2} s^{-1})[b]	10.8	3.30	1.2
$M(M_\odot)$	$1.17^{+0.05}_{-0.00}$	1.05 ± 0.01	1.20 ± 0.00
$Z^b(Z_\odot)$	$0.08^{+0.01}_{-0.02}$	0.06 ± 0.01	0.4
$EW_{\rm line}$[c] (eV)	163 ± 91	168 ± 92	166^{+95}_{-90}
$\cos(i)$	$0.97_{-0.822}$	$0.97_{-0.822}$	$0.97_{-0.822}$
χ^2_ν (dof)	1.00 (756)	1.06 (760)	1.11 (760)
R_m/R	39.0	24.7	37.0
h/R	3.89%	7.8%	4.75%
B (MG)	20.9	12.5	31.9
$kT_{\rm shock}$ (keV)	66.6	42.7	81.1

Notes. All errors shown are 90% confidence intervals. The three cases indicate three distinct fractional accretion area sizes.

[a] The ISM hydrogen column density associated with `tbabs`, which is applied to all models.

[b] Parameter is frozen.

[c] The equivalent width of the Gaussian component with $E = 6.4$ keV and $\sigma = 0.01$ keV for XMM-Newton data.

Consequently, the freefall velocity $v_{ff} = \sqrt{2GM\left(\frac{1}{R+h} - \frac{1}{R_m}\right)}$ (as well as plasma temperature and WD mass) becomes insensitive to changes in h, leading to a plateau of WD mass estimates. This is a systematic feature of the model rather than a physical phenomenon, and independent estimates of f are needed to place a more stringent constraint on WD mass. It also implies that the WD masses of IPs (or more generally mCVs) with higher specific mass accretion rates can be more tightly constrained.

Our results using the state-of-the-art spectral model `MCVSPEC` suggest ZTF J1851 possesses a massive and highly magnetized WD with $M = 1.07$–$1.32 M_\odot$ and $B = 20$–40 MG. The uncertainties are mainly attributed to the poorly constrained fractional accretion area. This places ZTF J1851 as one of the heavier IPs, above the mean WD mass $\langle M_{\rm WD} \rangle \approx 0.8 M_\odot$ of known IPs (A. F. Pala et al. 2022) and mCVs (A. W. Shaw et al. 2020). For some f values, our fitting suggests that ZTF J1851 may contain one of the most massive WDs close to the Chandrasekhar mass limit. The estimated magnetic field $B \gtrsim 20$ MG falls above a typical IP's B-field range of 0.1–10 MG (K. Mukai 2017). Note that the B-field range derived by assuming spin equilibrium represents an upper limit, because R_m can be smaller than the corotation radius R_{co}, as pointed out by V. F. Suleimanov et al. (2019, 2025). To consider how $R_m < R_{\rm co}$ affects the WD mass measurement, for a given f value ($f = 10^{-3}$ in this case), we repeated X-ray spectral fitting for a range of $R_m/R_{\rm co} = 0.2$–1 and found the WD mass to be floored at $M > 0.9 M_\odot$. The smaller R_m value reduces the free-falling distance between R_m and h, thereby lowering the shock temperature. On the other hand, the lower cyclotron cooling rate at lower B-field values keeps the overall plasma temperature higher in the accretion column. These counteracting effects lead to the minimum WD mass of $M = 0.9 M_\odot$, this being reduced from the lower bound of $M = 1.0 M_\odot$ (when $R_m = R_{\rm co}$) at $R_m/R_{\rm co} \approx 0.6$, corresponding to $B \sim 1$ MG. Therefore, if $R_m < R_{\rm co}$ is assumed, the WD mass estimate could be lower by ~10%, and this systematic effect will be addressed in our forthcoming `MCVSPEC` model paper (G. Bridges et al. 2025, in preparation).

6. Conclusion

We report the detection of a hard X-ray counterpart for ZTF J1851 and present the first investigation of the X-ray temporal and spectral properties of ZTF J1851. The broadband X-ray observations led to determining the intrinsic spin period and identifying the source as a massive IP with $M_{\rm WD} > 1 M_\odot$, assuming spin equilibrium. A combination of the soft and hard X-ray telescope data obtained by XMM-Newton, NICER, and NuSTAR enabled the measurements of the spin period and WD mass. Our spectral model `MCVSPEC` is the most self-consistent model that accounts for physical effects such as finite magnetospheric radius and X-ray reflection from the WD surface. Future observations of the source could improve the systematic uncertainty of our measurements by constraining f if they can detect a blackbody component, as well as better measuring other WD properties like mass and spin period derivative.

We also report six short (approximately day-long) optical outbursts over a course of nearly 7 yr. The outbursts are much shorter in duration than typical dwarf nova outbursts but similar in duration to those due to magnetic gating or from micronovae events (see K. Iłkiewicz et al. 2024 for a discussion). If we could confirm the day-long duration of optical outbursts in ZTF J1851 using multiple all-sky surveys or TESS data, then this would provide evidence for these bursts being caused by magnetic gating and therefore for the WD having a significant magnetic field. With a growing number of periodic sources discovered by optical and X-ray all-sky surveys (e.g., S. Mondal et al. 2024; A. D. Schwope et al. 2024), our results highlight the importance of follow-up broadband X-ray observations to identify periodic optical sources in the future. Similar X-ray follow-up observations could identify new CVs and UCBs through the current and future optical surveys (A. C. Rodriguez et al. 2025).

Acknowledgments

Support for this work was provided by NASA through NICER Cycle 4 (NNH21ZDA001N-NICER), XMM-Newton Cycle 22 (XMMNC22) Guest Observer program, and NASA ADAP program (NNH22ZDA001N-ADAP) grants. We thank Ciro Salcedo for his helpful discussions and contributions on timing analysis. GOTO (https://goto-observatory.org) is a network of telescopes that is principally funded by the STFC and operated at the Roque de los Muchachos Observatory on La Palma, Spain, and Siding Spring Observatory in NSW, Australia, on behalf of a consortium including the University of Warwick, Monash University, Armagh Observatory & Planetarium, the University of Leicester, the University of Sheffield, the National Astronomical Research Institute of Thailand (NARIT), the University of Turku, the University of Portsmouth, the University of Manchester, and the Instituto de Astrofisica de Canarias (IAC).

ORCID iDs

Ren Deng (邓仁) https://orcid.org/0009-0003-4151-7735
Kaya Mori https://orcid.org/0000-0002-9709-5389
Eric Miao https://orcid.org/0009-0009-6455-3804
Gabriel Bridges https://orcid.org/0000-0002-6653-4975
Charles J. Hailey https://orcid.org/0000-0002-3681-145X
David A. H. Buckley https://orcid.org/0000-0002-7004-9956
Gavin Ramsay https://orcid.org/0000-0001-8722-9710
Dan Jarvis https://orcid.org/0009-0004-3067-2227

References

Aizu, K. 1973, PThPh, 49, 1184
Arnaud, K. A. 1996, ASPC, 101, 17
Bachetti, M., 2018 HENDRICS: High ENergy Data Reduction Interface from the Command Shell, Astrophysics Source Code Library, ascl:1805.019
Bachetti, M., Huppenkothen, D., Stevens, A., et al. 2024, JOSS, 9, 7389
Bailer-Jones, C. A. L., Rybizki, J., Fouesneau, M., Demleitner, M., & Andrae, R. 2021, AJ, 161, 147
Bellm, E. C., Kulkarni, S. R., Graham, M. J., et al. 2019, PASP, 131, 018002
Burdge, K. B., Marsh, T. R., Fuller, J., et al. 2022, Natur, 605, 41
Dyer, M. J., Ackley, K., Jiménez-Ibarra, F., et al. 2024, SPIE, 13094, 130941X
Filor, L. W., Mori, K., Bridges, G., et al. 2025, ApJ, 987, 53
Frank, J., King, A., & Raine, D. J. 2002, Accretion Power in Astrophysics (3rd ed.; Cambridge Univ. Press)
Hailey, C. J., Mori, K., Perez, K., et al. 2016, ApJ, 826, 160
Harrison, F. A., Craig, W. W., Christensen, F. E., et al. 2013, ApJ, 770, 103
Hayashi, T., & Ishida, M. 2014, MNRAS, 438, 2267
Huppenkothen, D., Bachetti, M., Stevens, A. L., et al. 2019, ApJ, 881, 39
Iłkiewicz, K., Scaringi, S., Veresvarska, M., et al. 2024, ApJL, 962, L34
Joshi, A., Wang, W., Pandey, J. C., et al. 2022, A&A, 657, A12
Kato, T., & Kojiguchi, N. 2021, arXiv:2107.09913
Koliopanos, F., Péault, M., Vasilopoulos, G., & Webb, N. 2021, MNRAS, 501, 548
Lomb, N. R. 1976, Ap&SS, 39, 447
Magdziarz, P., & Zdziarski, A. A. 1995, MNRAS, 273, 837
Mondal, S., Ponti, G., Bao, T., et al. 2024, A&A, 686, A125
Mori, K., Chonko, J. C., & Hailey, C. J. 2005, ApJ, 631, 1082
Mukai, K. 2017, PASP, 129, 062001
Norton, A. J., Wynn, G. A., & Somerscales, R. V. 2004, ApJ, 614, 349
Pala, A. F., Gänsicke, B. T., Belloni, D., et al. 2022, MNRAS, 510, 6110
Patterson, J., Miguel, E. d., Kemp, J., et al. 2020, ApJ, 897, 70
Pietrukowicz, P., Mróz, P., Udalski, A., Soszyński, I., & Skowron, J. 2019, ApJL, 881, L41
Protassov, R., van Dyk, D. A., Connors, A., Kashyap, V. L., & Siemiginowska, A. 2002, ApJ, 571, 545
Ramsay, G., & Cropper, M. 2002, MNRAS, 334, 805
Ramsay, G., Hakala, P., Wu, K., et al. 2005, MNRAS, 357, 49
Rodriguez, A. C., El-Badry, K., Suleimanov, V., et al. 2025, PASP, 137, 014201
Rosen, S. R., Mason, K. O., & Córdova, F. A. 1988, MNRAS, 231, 549
Salcedo, C., Mori, K., Bridges, G., et al. 2024, ApJ, 976, 115
Scargle, J. D. 1982, ApJ, 263, 835
Scaringi, S., Bird, A. J., Norton, A. J., et al. 2010, MNRAS, 401, 2207
Schwope, A., Marsh, T. R., Standke, A., et al. 2023, A&A, 674, L9
Schwope, A. D., Knauff, K., Kurpas, J., et al. 2024, A&A, 690, A243
Shaw, A. W., Heinke, C. O., Mukai, K., et al. 2020, MNRAS, 498, 3457
Steeghs, D., Galloway, D. K., Ackley, K., et al. 2022, MNRAS, 511, 2405
Suleimanov, V., Doroshenko, V., Ducci, L., Zhukov, G. V., & Werner, K. 2016, MNRAS, 591, A35
Suleimanov, V. F., Doroshenko, V., & Werner, K. 2019, MNRAS, 482, 3622
Suleimanov, V. F., Ducci, L., Doroshenko, V., & Werner, K. 2025, A&A, 700, A180
Takata, J., Wang, X. F., Wang, H. H., et al. 2021, ApJ, 907, 115
Tonry, J. L., Denneau, L., Flewelling, H., et al. 2018, ApJ, 867, 105
Vermette, B., Salcedo, C., Mori, K., et al. 2023, ApJ, 954, 138
Wilms, J., Allen, A., & McCray, R. 2000, ApJ, 542, 914